Experimental demonstration of laser to x-ray conversion enhancements with low density gold targets

Wanli Shang,^{1,2} Jiamin Yang,^{1,*} Wenhai Zhang,¹ Yunsong Dong,¹ Zhichao Li,¹ Bo

Deng,¹ Tuo Zhu,¹ Chengwu Huang,¹ Xiayu Zhan,¹ Liang Guo,¹ Ruizhen Yu,¹ Sanwei Li,¹

Shaoen Jiang,¹ Shenye Liu,¹ Feng Wang,¹ Yongkun Ding,¹ Baohan Zhang,¹

Riccardo Betti²

¹Research Center of Laser Fusion, China Academy of Engineering Physics, P. O. Box 919-986,

Mianyang 621900, People's Republic of China

²Laboratory of Laser Energetics, Department of Physics, and Fusion Science Center, University of Rochester, 250 East River Road, Rochester, New York 14623-1299, USA

The enhancement of laser to x-ray conversion efficiencies by using low density gold targets [W. L. Shang et al. Appl. Phys. Lett. 102, 094105 (2013)] is demonstrated for the first time. Laser to x-ray conversion efficiencies with 6.3% and 12% increases are achieved with target densities of 1 and 0.25 g/cm³, when compared with that of a solid gold target (19.3 g/cm³). Experimental data and numerical simulations are in good agreement. The enhancement is caused by larger x-ray emission zone lengths formed in low density targets, which is in agreement with the simulation results.

Inertial confinement fusion (ICF) is an approach to fusion that relies on the inertia of the fuel mass to provide confinement. The indirect drive (ID) approach of ICF has attracted particular interest due to its relaxed requirement on laser beam uniformity [1,2]. Laser beams irradiate the inner wall of the hohlraum, and multiple absorption and reemission processes are responsible for the isotropization of the radiation field and the establishment of a uniform temperature in the hohlraum [3]. By these means the laser energy can be effectively absorbed and converted into near Planckian soft x-ray, which is then used to drive the capsule implosion inside the hohlraum [4,5]. As a consequence, the x-ray radiation in the hohlraum plays an important role in ID. Various methods have been proposed to enhance the x-ray drive in the hohlraum [6,7,8,9,10,11,12]. Shields were used to decrease the radiation losses at the laser entrance holes [6], special rugby-shaped hohlraum was utilized to replace the cylindrical shape leading to a significant energetic advantage [7,8], and mixture of high-Z wall materials (cocktails) [9,10] and gold foams [11,12] were adopted to reduce the x-ray losses into the hohlraum wall.

Most studies are focused on the radiation balance in the hohlraum and x-ray reemission efficiency of the hohlraum walls. The initial conversion efficiency of laser light into primary x-ray emission is also very important [12]. The incident laser energy is absorbed by electrons along the laser propagation in front of the critical surface through inverse bremsstrahlung absorption. Meanwhile, other physical processes occur, such as electron ion collision and equilibration, electron and ion thermal conduction, x-ray emission and radiation transport, and hydrodynamic flow [2].

According to our studies, laser energy deposition varies with target density for a given laser, and so does the coulomb collision between electrons and ions [13,14]. With an incident laser intensity of 5×10^{14} W/cm² (1ns flattop pulse and 351 nm wavelength), about 83% of the laser energy is absorbed for a solid gold target and 89% in the case of a 0.1 g/cm³ gold foam target. More electron ion collisions occur in the solid gold target than in the gold foam target because of the different particle density profiles. As a result, the gold foam plasma absorbs more energy but induces less ion kinetic energy, leading to higher x-ray emission [13]. Based on these results, we expect an increase in the conversion of laser to x-ray energy by using low density gold targets [13].

In this letter, we report on experiments demonstrating for the first time the enhancement of laser to x-ray CEs by using low density gold targets. However, the energy transfer to the ion kinetic energy is difficult to investigate experimentally. In our experiments x-ray emission zone lengths were measured, and corresponding simulations were performed. The experiments were conducted on the SGII laser facility [15]. The Beam #9 laser (\sim 500 J, \sim 1 ns, 351 nm, and flattop pulse) was used to irradiate targets with normal incidence. The beam was smoothed by a lens array, and the laser spot size was about 420×420 μ m, with laser intensity of around 3×10^{14} W/cm². The targets were gold layers with densities of 19.3, 1, and 0.25 g/cm³. The diagnostic system included an x-ray pinhole camera (XPHC), a transmission grating spectrometer (TGS) [16], a set of x-ray diodes (XRDs) [17], and an x-ray streak camera (XSC) [18]. The time integrated radiation spectra were measured with a space

resolved TGS, which was comprised of a 10 μ m spatial-resolution slit, a 50 μ m grating slit, a calibrated 2000 I/mm transmission grating, and a calibrated detecting charge-coupled device (CCD). The predicted spectral and spatial resolutions were 0.2 nm and 20 μ m. The XRDs gave the x-ray flux and x-ray angular distribution with temporal resolution of 250 ps. The corresponding spectrum ranges for the XRDs were 100-4000 eV. The XSC was used to investigate the time dependent plasma emission zone lengths at around 210 eV.

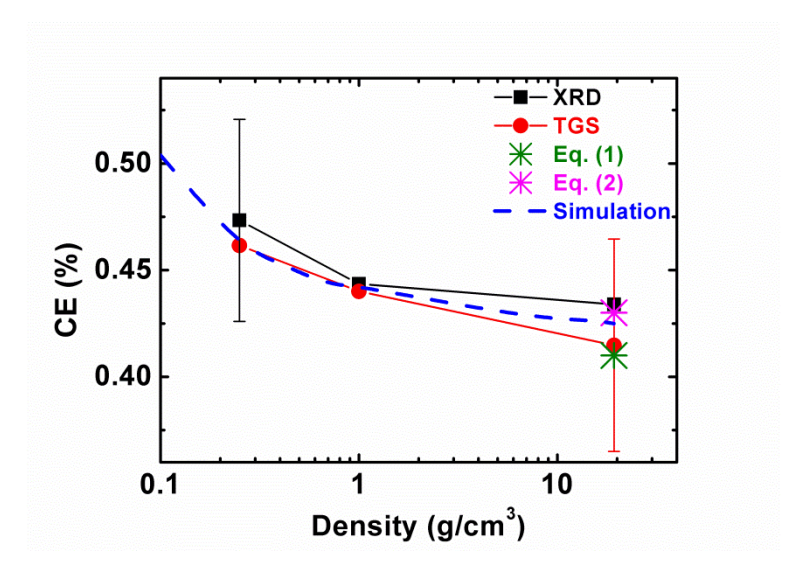


FIG. 1. Density dependent laser to x-ray conversion efficiency (CE= E_x/E_L) from XRDs, TGS, scaling laws (1) and (2), and simulations. Three gold targets with densities of 0.25 g/cm³, 1 g/cm³, and 19.3 g/cm³ were used in our experiments. The 1 ns flattop 351 nm laser intensity was around 3×10^{14} W/cm². The simulations were performed by 1D code Multi with a flux limiter of 0.03.

Figure 1 shows the laser to x-ray CE versus target density. The experimental CEs were obtained by XRDs and TGS. Five XRDs were used to obtain the x-ray angular distribution at 22.5°, 26.8°, 40.8°, 45°, and 68.3°. Since the x-ray angular distribution is neither isotropic nor Lambertian for laser irradiated planar targets, the x-ray angular distribution was fitted with a $\cos^{\alpha}\theta$ function. Integrating over the whole 2π stereoangle, the total emitted x-ray energy was calculated for evaluating the CE

($CE = E_x/E_L$) [19]. With the help of an iterative unfolding procedure, the primary spectrum of TGS was unfolded, and the space and time integrated spectrum could be acquired, and the CE could be attained with the given x-ray angular distribution by XRDs [19]. The CE error bars are less than 10% for XRDs and 12% for TGS [17,19].

It was reported, by examining x-ray spectra using XRDs and blackbody assumption, that for a solid gold planar target (19.3 g/cm 3), the radiation temperatures T_r as functions of laser intensity and wavelength could be inferred [20]. For a 351 nm wavelength laser, T_r and laser to x-ray CE could be as follows [20]:

$$\begin{cases}
T_r = 157I_{14}^{0.154} \\
CE = \sigma T_r^4 / I_{14}
\end{cases}$$
(1)

where σ is the Stefan-Boltzmann constant, the units of T_r and the laser intensity I_{14} are eV and 10^{14} W/cm². Within our experiments, Eq. (1) gives a radiation temperature of 185.9 eV for the gold target with density of 19.3 g/cm³, and then the CE can be obtained as 0.41. In addition, for the solid gold target, another scaling law for CE is provided experimentally [21]:

$$\begin{cases} \eta_a = 15.1 [\tau_{ns}^3 f / (I_0 \lambda_{\mu m}^8)]^{0.1} \\ CE = \eta_a 0.45 (I_{14} \lambda_{\mu m}^2)^{-0.15} \end{cases}$$
 (2)

where η_a is the absorption fraction of laser energy by plasma, τ_{ns} is the pulse duration in unit of ns, f is the flux limiter, I_0 is the laser intensity in unit of W/cm², $\lambda_{\mu m}$ is the wavelength in unit of μm , I_{14} is the laser intensity in unit of 10^{14} W/cm². Giving f as 0.03, which is the same as that used in previous studies [13,22], and using our experimental parameters, the CE for the 19.3 g/cm³ gold

target can be attained as 0.438.

The widely used one-dimensional (1D) multi-group radiation-hydrodynamics code Multi was used to simulate the laser to x-ray CE [23]. The hydrodynamic equations are solved in a Lagrangian formulation with coupled thermal radiation transport, heat conduction, and laser energy deposition mechanism of inverse bremsstrahlung. The equation of state (EOS) is taken from the SESAME library and opacity data are computed by SNOP [24]. Experimental parameters were adopted in the simulations and the flux limiter was set to 0.03. Time and spectrum integrated x-ray emission for 5 ns was calculated to determine the CE. The laser to x-ray CEs from experiments (both by XRDs and TGS), scaling laws (Eq. (1) and (2)), and simulations are in agreement at the density of 19.3 g/cm³. Note that the data in Fig. 1. Furthermore, the laser to x-ray CE increases as the gold target density decreases, in both the experiments and simulations. Illustrated by the case of TGS measurements, the x-ray CE increases from 0.414 to 0.44, and then to 0.463 while the target density decreases from 19.3 to 1, and then to 0.25 g/cm³, which means 6.3% and 12% enhancements are achieved when the gold target density is lowered.

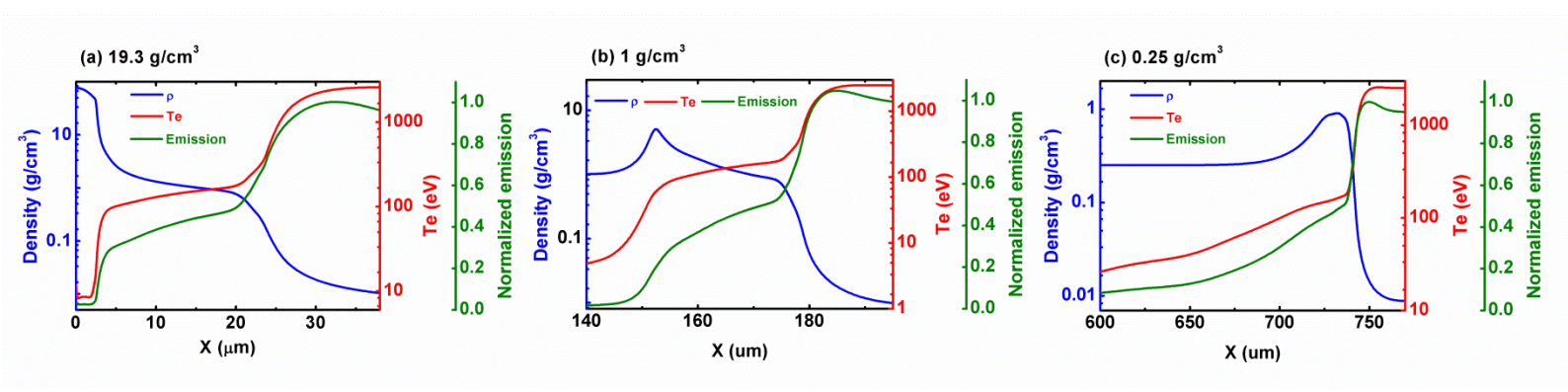


FIG. 2. Profiles of density $\,
ho$, electron temperature $\,T_{\!_e}$, and normalized emission intensity at 1 ns

with densities of 19.3, 1, and 0.25 g/cm³ (laser irradiates from right side).

Profiles of density ρ , electron temperature T_{e} , and normalized emission intensity with three different densities (19.3, 1 and 0.25 g/cm³) at 1 ns are presented in Fig. 2. For the 19.3 g/cm³ gold target, it is shown that there are three zones in laser-produced plasma: the corona, the electron thermal conduction zone, and the shock wave zone [25]. In the corona, laser energy is deposited to electrons, and then is transported inward by the electron thermal flux. In the electron conduction zone, plateaus of density and temperature develop. In this region, the radiation temperature, electron temperature, and ion temperature are almost equal, implying the local thermodynamic equilibrium [26]. Most of the x-ray emission occurs in the electron conduction zone because of the favorable temperature and densities, especially the lower energy x-ray of ~heV [27]. This situation can be seen clearly in Fig. 2(a) where a plateau of about 23 µm is shown (from the critical surface to the ablation front). The electron conduction zone (the plateau) shortens slightly as the target density changes to 1 g/cm3 in Fig. 2(b), and almost vanishes with density of $0.25 \text{ g/cm}^3 \text{ in Fig.2 (c)}.$

However, the reduction of the electron conduction zone does not lead to a decrease in x-ray emission. The reason for the increase of x-ray CE in Fig. 1 is because of an increase of the emission zone length, which can be defined as the distance that the emission would decrease to 10% of its peak x-ray emission (from the location of E_{peak} to $0.1E_{peak}$). Generally the peak x-ray emission locates around the critical surface [27]. In Fig. 2, the emission zone length changes from 27 to 39, and then to 309 μ m when target density decreases from 19.3 to 1, and then to 0.25 g/cm³, which

indicates a slight emission zone length increase from 19.3 to 1 g/cm^3 and a large increase from 1 to 0.25 g/cm^3 .

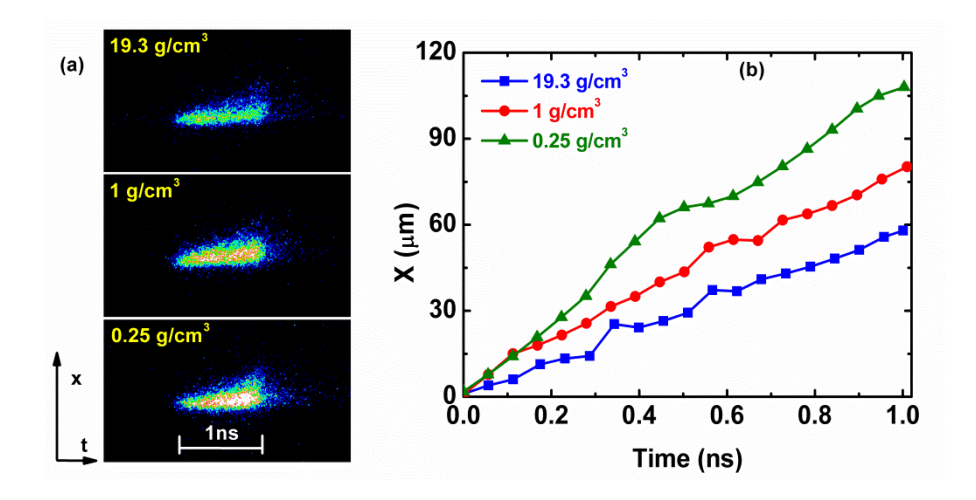


FIG. 3. Experimental x-ray emission zone length (X in the figures) versus time measured by XSC with densities of 19.3, 1, and 0.25 g/cm³.

Figure 3(a) shows the time dependent experimental emission zone length from the XSC. The XSC was set on lateral views and proper grating and slit were set to detect x-rays with photon energy around 210 eV. The illumination becomes brighter when the target density decreases (Fig. 3(a)). With the sweep speed calibration, we can obtain the time dependent data on emission zone lengths, defined as the distance between the two points exhibiting 10% of the peak x-ray emission. The data are shown in Fig. 3(b) [18]. At 1 ns, the emission zone length increases from 59 to 80, and then to 108 μ m when target density decreases from 19.3 to 1, and then to 0.25 g/cm³. The variation trend matches the simulation data, but the exact quantities are different. In the phase of density 19.3 to 1 g/cm³, the experimental emission zone lengths are bigger than the calculated results. The reason is that in simulations we only measure the emission zone length on the electron conduction zone side (from the location of E_{peak} to $0.1E_{peak}$), not the emission region on the other side

(corona), because most of the 210 eV x-ray (experimental measured photon energy) emitted on this zone. However, there is x-ray emission on the corona, even though most of the emission is high energy x-ray (above 1keV). Conversely, when the target density is 0.25 g/cm³, the experimental data falls below the calculated results (108 to 309 μ m). This is because the electron temperatures in the emission zones are different with different target densities. For instance, T_e at the inside boundaries of the emission zone (the location of $0.1E_{peak}$) is 100, 80, and 30 eV, corresponding to 19.3, 1, and 0.25 g/cm³ target. For x-ray radiation transport in gold plasma, the Planck mean free path is $I_p \propto T_e^{1.2}$ (Rosseland mean free path is $I_R \propto T_e$) [28]. As a result, with the lower target density (0.25 g/cm³), it is much more difficult for the x-ray generated near the inside boundary of the emission zone to escape the plasma, because of the lower photon mean free path. Therefore, the experimental emission zone length with target a density of 0.25 g/cm³ should be less than the calculated data (Fig. 2 and 3) due to the inhibited radiation transport to the detector.

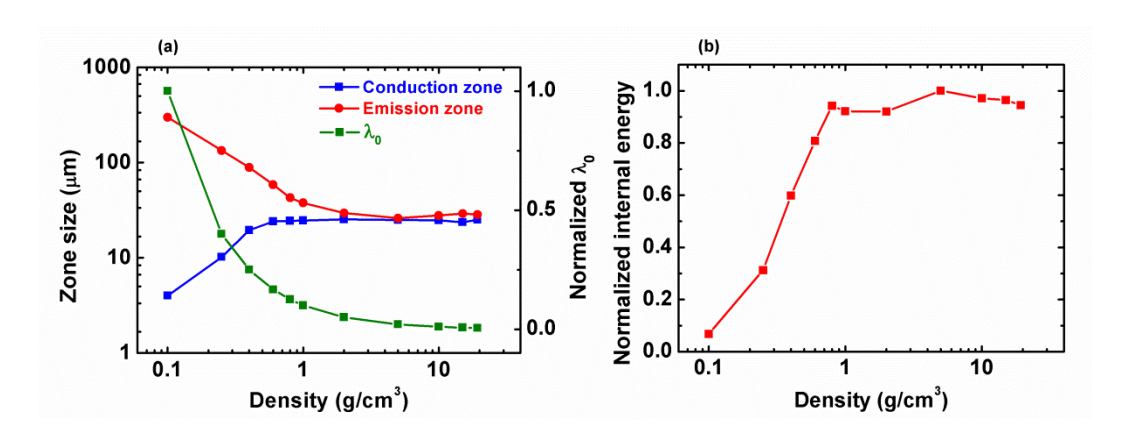


FIG. 4. (a) Calculated electron conduction zone length, x-ray emission zone length, and normalized electron mean free path λ_0 versus target density at 1 ns (normalized to the maximum λ_0); (b) Normalized internal energy of conduction zone versus target density (normalized to the maximum internal energy).

Electron conduction zone and x-ray emission zone lengths at 1 ns were calculated numerically and shown in Fig. 4(a). For the solid gold plasma (density of 19.3 g/cm³), it is mentioned above that most of the x-ray emission occurs in the electron conduction zone from the critical surface to the ablation front [25]. This implies the electron conduction zone is of similar length to the x-ray emission zone, and this characteristic can be seen clearly in Fig. 4(a), until the target density decreases to 1 g/cm³. As a result, gold plasmas have similar structures when the target density is over 1 g/cm³ (in Fig. 2(a) and (b)). However, with target density below 1 g/cm³, the electron conduction zone shortens significantly, while the x-ray emission zone grows quickly. At the density of 0.25 g/cm³, the electron conduction and x-ray emission zone lengths are 4 and 294 μm.

The electron mean free path is widely used to describe the distance that electron flux is transported, and it scales as $\lambda_0 \propto \frac{T_e^2}{n_e}$ by assuming a constant ionization stage and coulomb logarithm $\ln \Lambda$ [2,27]. T_e in the corona is dependent on the laser intensity and wavelength $T_e \propto \left(I\lambda^2\right)^{2/3}$ [2], leading to $\lambda_0 \propto \frac{\left(I\lambda^2\right)^{4/3}}{n_e}$. The normalized λ_0 is plotted in Fig. 4(a). Notice that there are two distinct regions: slowly varying λ_0 for higher density above 1 g/cm³, and significantly changing λ_0 for lower density below 1 g/cm³. X-ray emission would occur in the region of propagation of the electron thermal flux. Consequently, greater λ_0 leads to greater x-ray emission zone with density below 1 g/cm³. However, with this low target density, a new plasma structure is formed, while the electron can reach far before

the ablation front and the shock front, because of the significant λ_0 . Measured with the definition of electron conduction zone (from the critical surface to the ablation front) [25], shorter electron conduction zone lengths with the decreasing target density are demonstrated in this paper.

Specific internal energy is used to describe the plasma energetics and can be expressed as $e_0 \left(erg \, / \, g\right) \propto T_e \left(eV\right)^{1.6}$ for gold plasma [28]. Considering the internal energy e_c of the electron conduction zone in Fig. 4(a), we use the formula $e_c \propto e_0 \rho_c l_c \propto T_c^{1.6} \rho_c l_c$ in our 1D simulation, where T_c and ρ_c are the electron temperature and mass density at the center of the conduction zone, and l_c is the conduction zone length in Fig. 4(a). The normalized internal energy in the conduction zone is shown in Fig. 4(b). Greater internal energy is stored in the electron conduction zone for target density above 1 g/cm³ compared with that below 1 g/cm³, implying less emission in x-ray energy. As a result, for lower target density plasma, less energy is distributed to hold the electron conduction zone, and more x-ray emission is released.

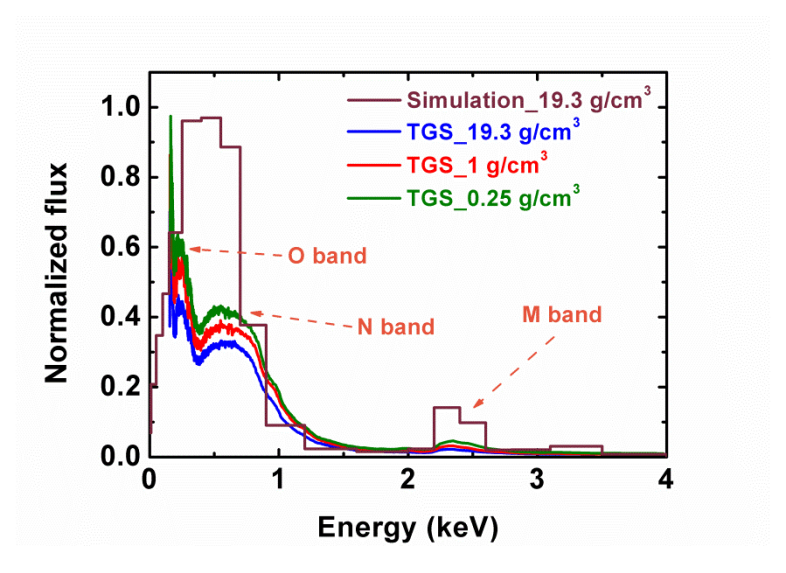


FIG. 5. Experimental time integrated spectra with target density of 19.3, 1 and 0.25 g/cm³ by TGS,

and numerical time integrated spectra with target density of $19.3~g/cm^3$ (normalized to the maximum flux).

Experimental and numerical spectra are presented in Fig. 5. Twenty photon groups are used in the simulation. Three x-ray groups are detected with TGS: the 200 eV -400 eV (31-62 Å) group, the 500-1000 eV (12.4-24.8 Å) group, and the 2000 -4000 eV (3.1-6.2 Å) group, which are O band, N band and M band emission groups of gold plasma respectively. Similar results with gold targets have been reported experimentally [29]. It can be seen that the numerical results agree qualitatively with the experimental data in the whole spectral range. However, it appears that the twenty photon group opacity data are not enough to resolve the O and N band x-ray emission. From TGS data we can find x-ray emission enhancements all through the spectral area, especially in the soft x-ray region below 1 KeV, which is the same with the numerical data [13].

In summary, we have demonstrated for the first time the enhancement of laser to x-ray CEs using low density gold targets in experiments. Planar gold targets with densities of 19.3, 1, and 0.25 g/cm³ were used. Laser to x-ray CE enhancements were achieved experimentally, which match the simulation data very well. Compared with the CE of the solid gold target (19.3 g/cm³), the TGS results show 6.3% and 12% increases for target densities of 1 and 0.25 g/cm³, respectively. Numerical data show that greater x-ray emission zone length can be attained when target density is lower, and SXC results validate it. In addition, the electron conduction zone shortens, and less internal energy is stored in the electron conduction zone with lower target density, leading to more energy released for x-ray emission. These results suggest

that a low density gold wall can be used to increase the x-ray drive in the hohlraum of ID ICF.

The authors are grateful to Dr. S. X. Hu and Dr. W. Theobald from the Laboratory of Laser Energetics, University of Rochester for many useful discussions. The authors are also grateful to the target manufacturers and the laser operation staff for their cooperation in this work. This work is performed under the auspices of the National Natural Science Fund of China (Grant No. 11305158).

This material is based upon work supported by the Department of Energy National Nuclear Security Administration under Award Number DE-NA0001944, the University of Rochester, and the New York State Energy Research and Development Authority. The support of DOE does not constitute an endorsement by DOE of the views expressed in this article.

- [1] J. Lindl, Phys. Plasmas. 2, 3933 (1995).
- [2] S. Atzeni and J. Meyer-ter-Vehn, The Physics of Inertial Fusion, Oxford: Clarendon, 2004.
- [3] S. H. Glenzer, B. J. MacGowan, P. Michel, N. B. Meezan, L. J. Suter, S. N. Dixit, J. L. Kline, G. A. Kyrala, D. K. Bradley, and D. A. Callahan et al., Science **327**, 1228 (2010).
- [4] J. D. Lindl, P. Amendt, R. L. Berger, S. G. Glendinning, S. H. Glenzer, S. W. Haan, R. L. Kauffman, O. L. Landen, and L. J. Suter, Phys. Plasmas. **11**, 339 (2004).
- [5] S. H. Glenzer, B. J. MacGowan, N. B. Meezan, P. A. Adams, J. B. Alfonso, E. T. Alger, Z. Alherz, L. F. Alvarez, S. S. Alvarez, and P. V. Amick et al., Phys. Rev. Lett. 106, 085004 (2011).
- [6] D. A. Callahan, P. A. Amendt, E. L. Dewald, S. W. Haan, D. E. Hinkel, N. Izurni, O. S. Jones, O. L. Landen, J. D. Lindl, and S. M. Pollaine et al., Phys. Plasmas 13, 056307 (2006).
- [7] M. Vandenboomgaerde, J. Bastian, A. Casner, D. Galmiche, J.-P. Jadaud, S. Laffite, S. Liberatore, G. Malinie, and F. Philippe, Phys. Rev. Lett. **99**, 065004 (2007).
- [8] F. Philippe, A. Casner, T. Caillaud, O. Landoas, M. C. Monteil, S. Liberatore, H. S. Park, P. Amendt, H. Robey, and C. Sorce et al., Phys. Rev. Lett. 104, 035004 (2010).
- [9] J. Schein, O. Jones, M. Rosen, E. Dewald, S. Glenzer, J. Gunther, B. Hammel, O. Landen, L. Suter, and R. Wallace, Phys. Rev. Lett. **98**, 175003 (2007).
- [10] O. S. Jones, J. Schein, M. D. Rosen, L. J. Suter, R. J. Wallace, E. L. Dewald, S. H. Glenzer, K. M. Campbell, J. Gunther, and B. A. Hammel et al., Phys. Plasmas. 14, 056311 (2007).
- [11] M. D. Rosen and J. H. Hammer, Phys. Rev. E 72, 056403 (2005).
- [12] P. E. Young, M. D. Rosen, J. H. Hammer, W. S. Hsing, S. G. Glendinning, R. E. Turner, R. Kirkwood, J. Schein, C. Sorce, and J. H. Satcher et al., Phys. Rev. Lett. 101, 035001 (2008).
- [13] W. L. Shang, J. M. Yang, and Y. S. Dong, Appl. Phys. Lett. 102, 094105 (2013).
- [14] Y. S. Dong, L. Zhang, J. M. Yang, and W. L. Shang, Phys. Plasmas. 20, 123102 (2013).
- [15] Z. Q. Lin, X. M. Deng, D. Y. Fan, S. J. Wang, S. H. Chen, J. Q. Zhu, L. J. Qian, X. H. Shen, F. M. Xu, and J. Zhu et al., Fusion Eng. Des. 44, 61 (1999).
- [16] W. L. Shang, T. Zhu, T. M. Song, W. H. Zhang, Y. Zhao, G. Xiong, J. Y. Zhang, and J. M. Yang, Phys. Plasmas. 18, 042705 (2011).
- [17] Z. C. Li, X. L. Zhu, X. H. Jiang, S. Y. Liu, J. Zheng, S. W. Li, Z. B. Wang, D. Yang, H. Zhang, L. Guo et al., Rev. Sci. Instrum. 82, 106106 (2011).
- [18] T. Zhu, J. M. Yang, B. Deng, D. Yang, X. He, and Z. B. Wang, Rev. Sci. Instrum. **81**, 056108 (2010).
- [19] W. L. Shang, H. Y. Wei, Z. C. Li, R. Q. Yi, T. Zhu, T. M. Song, C. W. Huang, and J. M. Yang, Phys. Plasmas. 20, 102702 (2013).
- [20] H. Nishimura, F. Matsuoka, M. Yagi, K. Yamada, S. Nakai, G.H. McCall, and C. Yamanaka, Phys. Fluids **26**, 1688 (1983).
- [21] S. E. Jiang, B. H. Zhang, S. Y. Liu, J. M. Yang, K. X. Sun, T. X. Huang, Y. K. Ding, and Z. J. Zheng, Science in China 37, 502 (2007).
- [22] W. C. Mead, E. M. Campbell, Kent Estabrook, R. E. Turner, W. L. Kruer, P. H. Y. Lee, B. Pruett, V. C. Rupert, K. G. Tirsell, and G. L. Stradling, et al., Phys. Fluids **26**, 2316 (1983).
- [23] R. Ramis, R. Schmalz, and J. Meyer-ter-Vehn, Comp. Phys. Comm. 49, 475 (1988).
- [24] K. Eidmann, Laser Particle Beams 12, 223 (1994).
- [25] F. Dahmani and T. Kerdja, Phys. Fluids B 3, 1232 (1991).
- [26] S. Li, High Temperature Radiation and Quantum Radiation Physics, National Defence Industry

- Press, 1992.
- [27] J. Zhang and T. Chang, Fundaments of the Targets Physics for Laser Fusion, National Defense Industry Press, 2004.
- [28] M. Murakami, J. Meyer-ter-Vehn, and R. Ramis, J. X-ray Sci. Technol. 2, 127 (1990).
- [29] E. L. Dewald, M. Rosen, S. H. Glenzer, L. J. Suter, F. Girard, J. P. Jadaud, J. Schein, C. Constantin, F. Wagon, and G. Huser et al., Phys. Plasmas. **15**, 072706 (2008).